Contents lists available at ScienceDirect

Organic Electronics

Cyano substitution effect on the emission quantum efficiency in stilbene derivatives: A computational study

Tian Zhang[a,*], Guozheng Zhu[a], Lili Lin[b], Jinglin Mu[a], Bing Ai[a], Yuchao Li[a], Shuping Zhuo[a,**]

[a] School of Chemistry and Chemical Engineering, Shandong University of Technology, Zibo, 255049, PR China
[b] Shandong Province Key Laboratory of Medical Physics and Image Processing Technology, Institute of Materials and Clean Energy, School of Physics and Electronics, Shandong Normal University, Jinan, 250014, PR China

ABSTRACT

A series of cyano-substituted stilbene derivatives exhibit quenched fluorescence in solution, in sharp contrast to their highly emissive parent counterparts. By employing the polarizable continuum model (PCM) method coupled with thermal vibration correlation function (TVCF) formalism, we comparatively investigated the electronic structures and excited-state dynamics of cyano-substituted *para*-distyrylbenzene (CN-DSB), 1,2-bis (pyridylphenyl)ethane (CN-BPPE) and the corresponding non-substituted DSB and BPPE lack of the cyano groups at their vinylene moieties in solution. The results show that the non-radiative decay rate constants of the CN-substituents are greatly enhanced by more than 4 orders of magnitude, while the radiative decay rate constants experience slight reduction, resulting in the very tiny fluorescence quantum efficiency. By analyzing the re-organization energies projected onto both normal modes and internal coordinates, the non-radiative consumption ways via molecular torsional motions of the single even double bonds adjacent to the CN group are active upon CN-substitution. Our study presents a rational explanation for the experimental CN-substitution induced quenching phenomena in stilbene derivatives, which is beneficial for the design of new fluorescent emitters and probes.

1. Introduction

Organic π-conjugated fluorescent molecules have attracted great attention for their optoelectronic and biophotonic applications [1–6]. One typical class of the π-conjugated skeletons contains the stilbene unit, which exhibits electronic delocalization with sp^2-hybridized carbon atom on the double bond and π electron on the benzene ring [7,8]. Diverse selection of the substituents at the stilbene units allows for modulation of the electronic structure and thus the photophysical properties of the resulting conjugates. The introduction of the electron-withdrawing cyano (CN) group in the double bond of the stilbenic moiety has been found to be a general emission quenching manner in solution. Such phenomena were earlier observed in addition of the CN substituents at the vinylene moieties of oligophenylenevinylenes [9]. Then, they were found to be widely present in the stilbene derivatives. For example, 1-cyano-*trans*-1,2-bis-(4′-methylbiphenyl)-ethylene (CN-MBE) is non-emissive in tetrahydrofuran with the fluorescence quantum efficiency (Φ_f) as low as 0.1% but *trans*-4,4′-diphenylstilbene (DPST) lack of the CN group emits brightly [10]. Functionalizing the

vinylene units of *para*-distyrylbenzene (DSB) with CN groups either in the inner (α)- or outer (β)-position causes remarkable emission quenching in trichloromethane (CHCl$_3$) [11,12]. Recently Gierschner and Park also reported several emissive stilbene derivatives containing β-CN-DSB moieties but additional alkoxy-substituents in phenyls are necessary [12]. CN-substituted 1,2-bis(pyridylphenyl)ethene (CN-BPPE) shows almost no fluorescence in dichloromethane (CH$_2$Cl$_2$) (Φ_f = 0.2%), while the non-substituted BPPE exhibits intense emission (Φ_f = 97%) [13]. Similarly, CN-substituted oligo(*para*-phenylene vinylene) (DP-β-CN-DSB) [14], carbazole-substituted α-CN-DSB (Cz-α-CN-DSB) [15], 2,3,3-triphenylacrylonitrile (TPAN) [16] and the architectures based on above cyanostilbene elements [17,18] are all poorly luminescent in dilute solution ($\Phi_f \approx$ 1%). The fluorescence quenching behaviors induced by CN-substitution are quite intriguing. The twisted conformation and the occurrence of conical intersection in the CN-substituted chromophores have been supposed to be the origin [10,12]. However, other excited-state deactivation pathways have been rarely concerned. It is primarily the purpose of this work to investigate the excited-state dynamics of the CN-substituted stilbenoid systems at the

---

* Corresponding author.
** Corresponding author.
  E-mail addresses: tzhang@sdut.edu.cn (T. Zhang), zhuosp_academic@yahoo.com (S. Zhuo).

Table 1

Selected dihedral angles (in deg, marked in Chart 1) of DSB, $\alpha(\beta)$-CN-DSB, BPPE and CN-BPPE in solution. S_0/S_1 and Δ represent the geometric parameters extracted from the optimized S_0/S_1 states and the difference between them, respectively. Torsional angles with larger modifications upon excitation are displayed in bold.

	S0	S1	Δ	S0	S1	Δ	S0	S1	Δ	S0	S1	Δ	S0	S1	Δ
	DSB			α-CN-DSB			β-CN-DSB			BPPE			CN-BPPE		
1-	−0.44	0.00	0.44	12.13	4.79	7.34	29.26	13.20	**16.06**	33.44	19.49	13.95	33.83	21.20	12.63
2-	−0.52	0.00	0.52	27.86	5.46	**22.40**	11.16	5.01	6.15	−1.73	−0.03	1.70	9.70	7.79	1.91
3-	−0.47	0.00	0.47	−27.86	−5.46	**22.40**	−11.16	−5.01	6.15	−1.73	−0.03	1.70	27.65	8.98	**18.67**
4-	−0.37	0.00	0.37	−12.13	−4.79	7.34	−29.26	−13.20	**16.06**	33.44	19.49	13.95	34.01	24.92	9.09
5-	−0.09	0.00	0.09	3.57	4.50	0.93	3.49	7.26	3.77	−0.07	−0.19	0.12	3.38	19.03	**15.65**
6-	−0.08	0.00	0.08	−3.57	−4.50	0.93	−3.49	−7.26	3.77						

first-principles level and explore the quenching mechanism.

Herein, we carried out detailed computational studies on the photophysical properties of DSB, $\alpha(\beta)$-CN-DSB, BPPE and CN-BPPE (Chart 1). The solvent environment was modelled by using the polarizable continuum model (PCM). The vibrationally resolved fluorescence spectra and excited-state decay rate constants were computed by the multimode coupled thermal vibration correlation function (TVCF) formalism. Our theoretical work gains deeper insight into the CN-substitution effect on the emission quantum efficiency in stilbene derivatives.

2. Computational method

Geometry optimizations and frequency calculations were performed by using density functional theory (DFT) for the ground (S_0) state and time-dependent DFT (TD-DFT) for the lowest excited singlet (S_1) state with the PBE0 [19] functional and 6-31G(d) basis set, the level of which has been proven to be reliable to study the electronic structures of the organic π-conjugated fluorescent molecules [20,21]. As the excited-state properties are functional dependent, we then recalculate the excitation energies employing different functionals based on the optimized structures taking the example of DSB, and results were presented in Table S1. Finally, we adopted BMK [22] functional to better match the experimental absorption and emission maxima. In the PCM setup (Chart 2), the equilibrium solvation approach was applied for geometry optimizations and the non-equilibrium solvation one was used for single-point calculations at the optimized geometries [23]. The state-specific method was chosen to compute the excited-state transition properties [24]. All above calculations were carried out with the Gaussian 16 package [25].

The molecular light-emitting efficiency Φ_f is determined by the competition between the radiative decay rate (k_r) and non-radiative decay rate (k_{nr}) with the equation of $\Phi_f = k_r/(k_r + k_{nr})$. k_{nr} consists of the internal conversion rate (k_{ic}) and intersystem crossing rate (k_{isc}). To evaluate the magnitude of k_{isc}, we calculated the energy differences and the spin-orbit coupling (SOC) constants between S_1 and T_1 at the TD-PBE0/6-31G(d) level based on the S_1-optimized geometry. The SOC matrix elements were derived from the exact two-component Hamiltonian as implemented in BDF program [26]. We found that the S_1-T_1 energy differences are considerably large (> 1.4 eV) and the SOC constants are quite small (< 0.1 cm^{-1}) (Table S2), and therefore k_{isc} can be neglected for the stilbenoid systems investigated in our work. On the basis of the electronic structure and Hessian information of the S_0 (S_1) states obtained from (TD)-DFT calculations, we calculated the optical spectra, k_r and k_{ic} with the TVCF formalism implemented in the Molecular Materials Property Prediction Package (MOMAP) [27], in which the photophysics module shows superiority in predicting the optical properties of organic π-conjugated molecules [28].

The analytical formalism we adopted to obtain the photoluminescence spectrum can be written as:

$$\sigma_{em}^{FC}(\omega, T) = \frac{2\omega^3}{3\pi\hbar c^3} |\vec{\mu}_0|^2 \int_{-\infty}^{\infty} e^{-i(\omega-\omega_{if})t} Z_i^{-1} \rho_{em,0}^{FC}(t, T) dt \tag{1}$$

where $\vec{\mu}_0$ is the electric transition dipole moment, which is independent of the nuclear coordinate under the Franck-Condon (FC) approximation. Z_i is the partition function and $\rho_{em,0}^{FC}(t, T)$ is the correlation function. Integration over the whole emission spectrum, $k_r(T) = \int \sigma_{em}^{FC}(\omega, T) d\omega$.

Within the framework of the Fermi Golden rule, the analytical formalism for k_{nr} can be expressed as:

$$k_{nr} = \sum_{kl} \frac{1}{\hbar^2} R_{kl} \int_{-\infty}^{\infty} dt \left[e^{i\omega_{if}t} Z_i^{-1} \rho_{ic,kl}(t, T) \right] \tag{2}$$

where $\rho_{ic,kl}(t, T)$ is the correlation function part. The non-adiabatic electronic couplings related to R_{kl} were treated as the force acting on the atomic nuclei based on the first-order perturbation theory following Lin [29]. The transition electric field was computed at the TD-PBE0/6-31G(d) level using the Gaussian 16 package. More methodology details on these formulas can be found in Peng's and Shuai's studies [30–32].

Normal mode analyses related to the above excited-state deactivation pathways were done with the EVC module embedded in the MOMAP program.

3. Results and discussion

3.1. Geometric structure and transition property

Geometric parameters with major differences between S_0 and S_1 are listed in Table 1. Atom index related to the labeled dihedral angles is given in Fig. S1. Compared with the pristine systems, torsional motions around the single and double bonds (Chart 1) in the CN-substituents are more significant. The dihedral angles at 2,3-positions in α-CN-DSB and 1,4-positions in β-CN-DSB exhibit great variations of 22.40° and 16.06° upon excitation, far larger than those in DSB of ~0.5°. The torsional angles at 3- and 5-positions in CN-BPPE show biggest changes of 18.67° and 15.65°, compared to BPPE with the values of 1.70° and 0.12°. This indicates remarkable geometry relaxations in the $S_1 \rightarrow S_0$ IC process for the CN-substituents. Largest geometry modifications occur at the single bonds adjacent to the CN group for $\alpha(\beta)$-CN-DSB and appear at both the single and double bonds connected to the CN group for CN-BPPE. Different from $\alpha(\beta)$-CN-DSB, the extra rotation of the double bond in CN-BPPE stems from substantial reorganization of pyridyls attached to the central stilbene core. In addition, all torsional angles at S_0/S_1-geometries for the CN-substituents are always much larger than the non-substituted ones, indicating that the CN-substituents possess more twisted structures.

Calculated vertical transition energies (ΔE_{vert}) at the S_0 and S_1 minima, electric transition dipole moments (μ), oscillator strengths (f), as well as available experimental absorption and emission maxima are listed in Table 2. The TD-DFT calculations reproduce reasonably well the experimental data with the largest deviation being 0.16 eV. Both calculations and experiments show that the emission peaks are remarkably red-shifted for the CN-substituents than the pristine counterparts but the absorption shifts are minor or slightly blue-shifted, implying larger Stokes shifts. The calculated Stokes shifts and adiabatic

Table 2
Calculated vertical transition energies (ΔE_{vert}) related to absorption (abs.) and emission (emi.) peaks as well as the experimental (exp.) values, electric transition dipole moments (μ), oscillator strengths (f) and HOMO→LUMO components for DSB, $\alpha(\beta)$-CN-DSB, BPPE and CN-BPPE in solution.

		ΔE_{vert}	exp.	μ	f	HOMO→LUMO
DSB	abs.	3.54 eV (350 nm)	3.48 eV (356 nm)[a]	12.24 D	1.88	99.7%
	emi.	3.00 eV (413 nm)	3.01 eV (412 nm)[a]	13.68 D	2.02	99.7%
α-CN-DSB	abs.	3.58 eV (346 nm)	3.61 eV (343 nm)[a]	10.57 D	1.41	99.5%
	emi.	2.92 eV (425 nm)	2.93 eV (423 nm)[a]	12.52 D	1.63	99.6%
β-CN-DSB	abs.	3.30 eV (376 nm)	3.46 eV (358 nm)[a]	11.32 D	1.50	99.6%
	emi.	2.69 eV (461 nm)	2.77 eV (448 nm)[a]	13.16 D	1.69	98.7%
BPPE	abs.	3.72 eV (333 nm)	3.59 eV (345 nm)[b]	11.76 D	1.83	99.3%
	emi.	3.06 eV (405 nm)	3.04 eV (408 nm)[b]	13.57 D	2.03	99.7%
CN-BPPE	abs.	3.64 eV (341 nm)	3.61 eV (343 nm)[b]	10.41 D	1.40	99.2%
	emi.	2.84 eV (437 nm)	2.79 eV (444 nm)[b]	12.04 D	1.48	99.9%

[a] In CHCl$_3$ [12].
[b] In CH$_2$Cl$_2$ [13].

Table 3
Calculated Stokes shifts and adiabatic excitation energies (ΔE_{ad}) as well as the related experimental (exp.) values for DSB, $\alpha(\beta)$-CN-DSB, BPPE and CN-BPPE in solution.

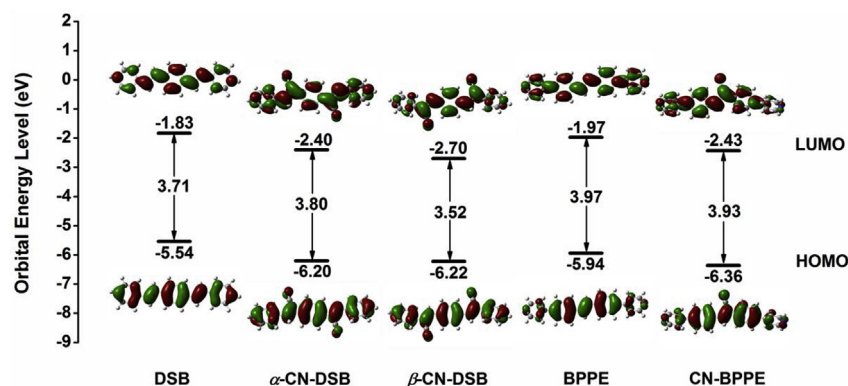|	Stokes shift	exp.	ΔE_{ad}	exp.
DSB	0.54 eV (63 nm)	0.47 eV (56 nm)	3.29 eV (377 nm)	3.26 eV (380 nm)
α-CN-DSB	0.66 eV (79 nm)	0.68 eV (80 nm)	3.24 eV (383 nm)	3.24 eV (383 nm)
β-CN-DSB	0.61 eV (85 nm)	0.69 eV (90 nm)	3.02 eV (410 nm)	3.05 eV (407 nm)
BPPE	0.66 eV (72 nm)	0.55 eV (63 nm)	3.40 eV (365 nm)	3.31 eV (375 nm)
CN-BPPE	0.80 eV (96 nm)	0.82 eV (101 nm)	3.26 eV (380 nm)	3.13 eV (396 nm)

Fig. 1. Calculated orbital energy levels, energy gaps and electron density contours of HOMOs and LUMOs for DSB, $\alpha(\beta)$-CN-DSB, BPPE and CN-BPPE at their S$_0$ equilibrium geometries in solution.

excitation energies (ΔE_{ad}) given in Table 3 agree even better with the experimental values. The experimental adiabatic energies are approximated by the intersection between the absorption and emission spectra. The Stokes shifts are larger upon CN substitution but the adiabatic excitation energies, μ and f are smaller. It also can be seen from Table 2 that their S$_1$ states are dominated by the strong-dipole allowed transitions from HOMO to LUMO with the components of > 98%. The corresponding landscapes of HOMO and LUMO as well as their energies are shown in Fig. 1. The HOMOs demonstrate π character and the LUMOs display π^* feature. The HOMO-LUMO energy gaps at their S$_0$ equilibrium geometries follow the order of β-CN-DSB < DSB < α-CN-DSB and CN-BPPE < BPPE, in accord with the absorption maxima energies. The introduction of the CN group causes both decreased LUMO levels and increased structural twists. In most cases, the more strongly stabilized LUMO overwhelms the opening of the HOMO-LUMO gaps due to the twisted structure and narrows the gaps. An exception is α-CN-DSB, where the steric effect dominates.

3.2. Excited-state decay and quantum efficiency

Calculated and experimental room-temperature optical emission spectra are shown in Fig. 2. Note that the spectrum lineshape naturally originates from the vibronic structure and temperature effect, without any extra broadening. The theoretical vibrationally resolved fluorescence spectra agree well with the experimental line shapes, which confirm the reliability of the TVCF formalism and PCM approaches adopted in this work. Compared to the parent compounds, the CN-substituents exhibit red-shifted emission bands with the loss of significant vibronic feature in both theory and experiments. This implies that the CN-substituents are more flexible.

Calculated and experimental excited-state decay rate constants (k_r and k_{nr}) and the fluorescence quantum efficiency (Φ_f) are listed in Table 4. In order to eliminate the oscillation feature of the numerical integration for the correlation function in some finite systems, the Lorentz broadening is included in the k_{nr} calculations following Niu [31]. The broadening width (FWHM) of 10.60 cm^{-1} is adopted for all compounds to ensure unity and convergence of the correlation function. It should be mentioned that the FWHM value influences the k_{nr}
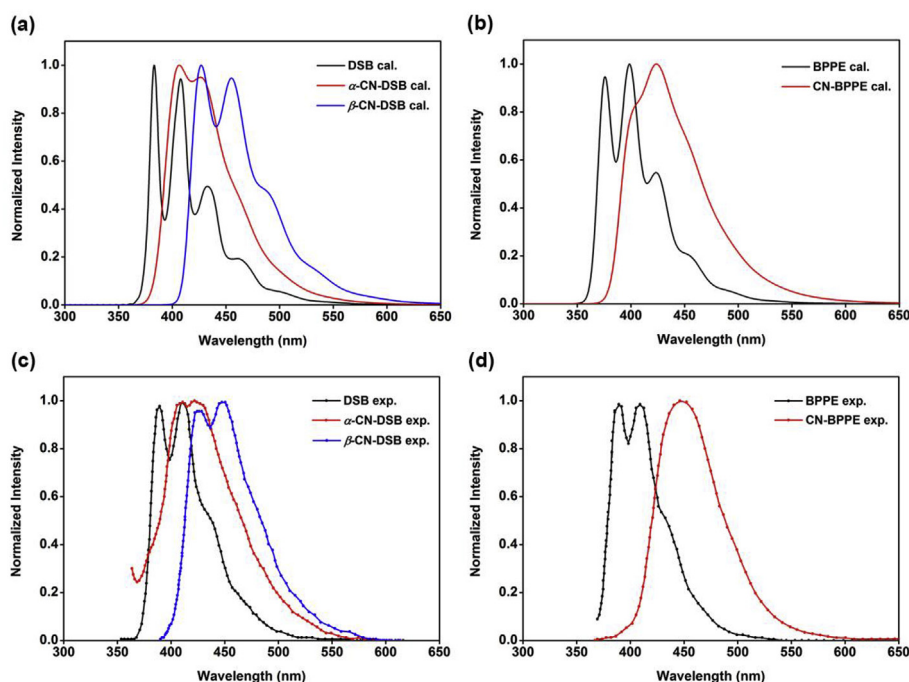
Fig. 2. Calculated (cal., a, b) and experimental (exp., c, d) optical emission spectra for DSB, $\alpha(\beta)$-CN-DSB, BPPE and CN-BPPE in solution (T = 298 K).

Table 4
Calculated k_r, k_{nr} and Φ_f for DSB, $\alpha(\beta)$-CN-DSB, BPPE and CN-BPPE in solution (T = 298 K). Corresponding experimental values are also presented in parentheses.

	k_r (s^{-1})	k_{nr} (s^{-1})	Φ_f
DSB	8.1×10^8 (7.1×10^8)	2.1×10^7 (8.0×10^7)	97% (90%)
α-CN-DSB	6.0×10^8 (3.5×10^8)	1.8×10^{11} (1.8×10^{11})	0.33% (0.2%)
β-CN-DSB	5.5×10^8 (4.5×10^8)	1.6×10^{11} (4.5×10^{10})	0.34% (1%)
BPPE	8.6×10^8 (1.1×10^9)	2.4×10^7 (3.5×10^7)	97% (97%)
CN-BPPE	5.3×10^8 ($> 2.0 \times 10^7$)	1.0×10^{11} ($> 1.0 \times 10^{10}$)	0.52% (0.2%)

value significantly for relatively rigid compounds as DSB and BPPE (Table S3), but hardly affects that of the cyano-substituted ones because large low-frequency electron-vibration couplings favor converged correlation function [32]. Therefore, only qualitative conclusion can be drawn based on a united FWHM values. Calculated results with FWHM = 10.60 cm^{-1} are in good agreement with the experiments. For the CN-substituents, k_r is slightly decreased (< 50%) and k_{nr} is increased by more than 4 orders of magnitude compared to the parent compounds, leading to the largely decreased Φ_f and emission quenching. According to the Einstein spontaneous emission equation, k_r is proportional to the oscillator strength and vertical emission energy ($k_r \sim f\Delta E_{vert}^2$). Since the oscillator strength has a proportional relationship with the square of the electric transition dipole moment ($f \sim \mu^2$), we then evaluated μ from S$_1$ to S$_0$ at S$_1$-optimized geometries and their vectors are plotted in Fig. S2. It is found that the values of μ decrease upon CN-substitution as the x-component along the orientation of the stilbene skeleton is reduced. Compared to the parent compounds, there also exists significant reduction in the vertical emission energies for the CN-substituents (Table 2). Finally, both the reduced electric transition dipole moments and vertical emission energies give rise to the decreased k_r via CN-substitution. To figure out the reason why the values of k_{nr} of the CN-substituents are several orders of magnitude larger than that of the pristine systems, we plotted the log (k_{nr}) as a function of the energy gap ΔE for DSB, $\alpha(\beta)$-CN-DSB, BPPE and CN-BPPE (Fig. 3). When ΔE equals to the adiabatic excitation energy ΔE_{ad}, the corresponding

value is k_{nr}. According to the k_{nr} formula in Eq. (2) and the energy gap law [29,31,32], the non-adiabatic electronic couplings, ΔE_{ad} and reorganization energies are three important factors to determine k_{nr}. As can be seen from Fig. S3, the non-adiabatic coupling terms hardly vary upon CN-substitution. As far as ΔE_{ad} is concerned, it goes down from DSB to $\alpha(\beta)$-CN-DSB and BPPE to CN-BPPE, resulting in the slight increase of k_{nr} but the magnitude is less than one order assuming the parabolas remain unchanged (Fig. 3). Finally, the reorganization energy mainly governs k_{nr}. The parabolas become broader with the increase of the reorganization energy λ. According to the adiabatic potential energy surface method, λ corresponds to the Stokes shift in Table 3. It can be seen that λ of $\alpha(\beta)$-CN-DSB is larger than DSB and CN-BPPE is larger than BPPE. Therefore, the parabolas get far broader for the CN-substituents than the parent compounds, leading to the final dominant decrease in k_{nr}.

3.3. Reorganization energy in mode and geometry relaxations

λ can be expressed as a summation of λ_g and λ_e. λ_g and λ_e are the reorganization energies in the ground (g) and excited (e) states. Under the harmonic oscillator approximation, $\lambda_{g(e)}$ can also be projected onto mode relaxations with the definition of $\lambda_{g(e)} = \sum_{j \in g(e)} \lambda_j = \sum_{j \in g(e)} \hbar S_j \omega_j$. S_j is the Huang-Rhys factor, which characterizes the electron-vibration coupling strength of the j-th normal mode. $\lambda_{g(e)}$ increases upon CN-substitution (Table S4). To measure the non-radiative energy consumption channels, we plot λ_j of each normal mode as well as displacement vectors of significant modes with major reorganization energies in Fig. 4. There are two vibration regions that are very important in the non-radiative energy relaxation process, identified as areas of low-frequency (LF, < 200 cm^{-1}) and high-frequency (HF, 1400−1800 cm^{-1}) modes. It can be seen that the LF modes are redshifted upon CN-substitution, e.g., 149 cm^{-1} in DSB to 55, 66, 93, 133 cm^{-1} in α-CN-DSB and 43 cm^{-1} in β-CN-DSB. Correspondingly, the contribution of all LF modes to the total is ∼9 meV (3%) in DSB, whereas it increases to ∼107 meV (31%) and 58 meV (20%) in α-CN-DSB and β-CN-DSB, respectively. However, the proportion of all HF modes to the total experiences slight reduction upon CN-substitution due to the almost unchanged numerator and largely increased
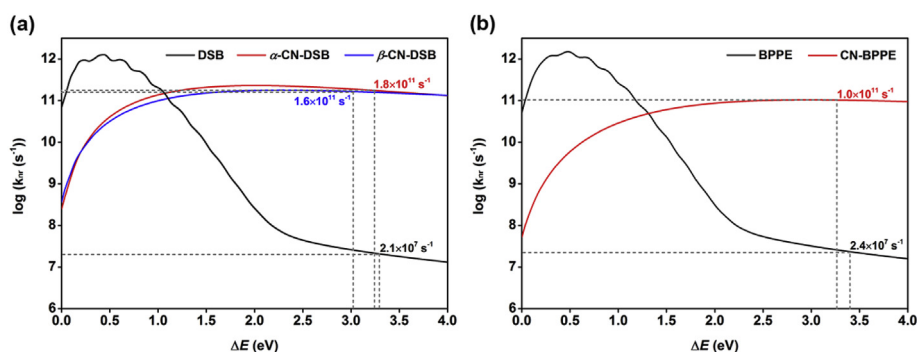
Fig. 3. Calculated non-radiative decay rate k_{nr} versus the energy gap ΔE for DSB (a), $\alpha(\beta)$-CN-DSB (a), BPPE (b) and CN-BPPE (b) in solution. The vertical dash line indicates the position of the adiabatic energy gap ΔE_{ad}.

denominator (Table S5). Similar cases also occur in BPPE and CN-BPPE. It also can be seen from Tables S6–S7 that S_j of the LF modes are much larger for the CN-substituents than the parent compounds. Therefore, the increase in $\lambda_{g(e)}$ upon CN-substitution mainly stems from the increased S_j of the LF modes since ω_j decreases. These LF modes are mainly assigned to the out-of-plane motions of phenyls adjacent to the CN groups in $\alpha(\beta)$-CN-DSB (Table S6) and rotational movements of the single and double bonds connected to the CN group in CN-BPPE (Table S7).

To elaborate the relationship between energy dissipation and molecular structure, we project the reorganization energy onto geometry relaxations in internal coordinates [31,33]. Contributions from bond length, bond angle and dihedral angle are shown in Fig. 5. Corresponding data are presented in Tables S8–S10. Upon CN-substitution, the contribution from bond length decreases as the denominator of total reorganization energies increases, while the contribution from bond
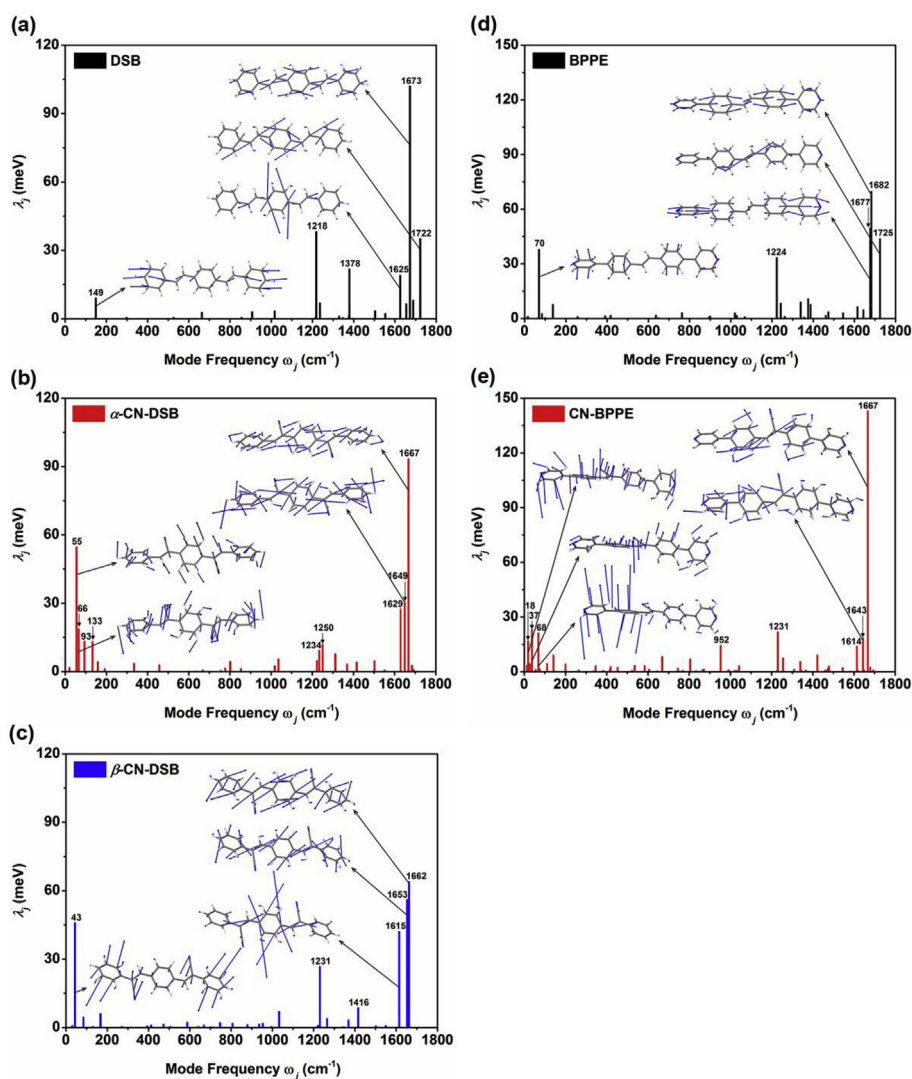

Fig. 4. Projection of the reorganization energy onto mode relaxations for DSB (a), $\alpha(\beta)$-CN-DSB (b, c), BPPE (d) and CN-BPPE (e) in solution.
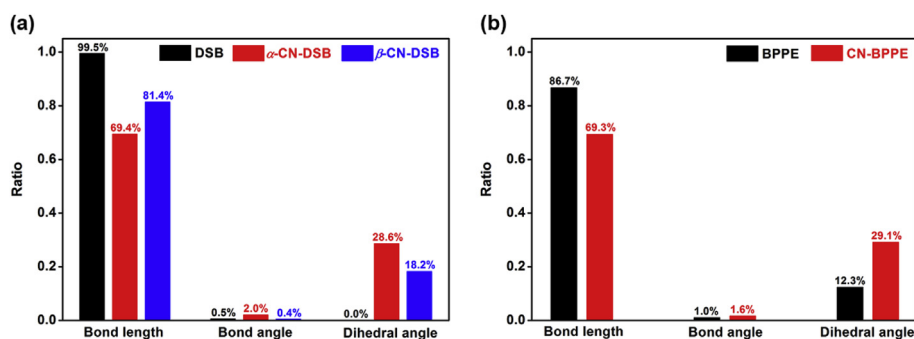
Fig. 5. Projection of the reorganization energy onto geometry relaxations (bond length, bond angle and dihedral angle) for DSB (a), *α(β)*-CN-DSB (a), BPPE (b) and CN-BPPE (b) in solution.
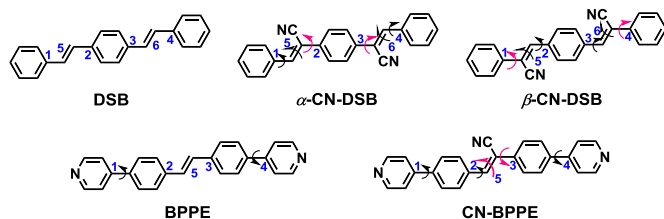

Chart 1. Molecular structures of DSB, *α(β)*-CN-DSB, BPPE and CN-BPPE (torsional angles are marked by numbers and arrows).
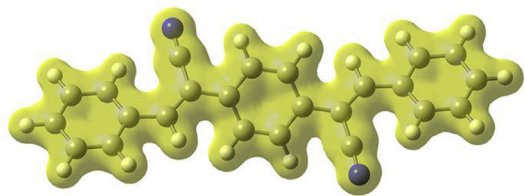

Chart 2. Setup of PCM model (take *α*-CN-DSB as an example).

angle experiences slight change. Notably, the contribution from dihedral angle is increased by ca. 20%–30%. Thus, the increase in $\lambda_{g(e)}$ via CN-substitution mainly originates from the increment contributed by the dihedral angle. The main components of the increment are dihedral angles at 2,3-positions in *α*-CN-DSB, 1,4-positions in *β*-CN-DSB and 3,5-positions in CN-BPPE (Table S11), which correlate to the torsional motions of the single even double bonds neighbouring the CN group.

4. Conclusions

In conclusion, we have theoretically investigated the emission quenching effect caused by cyano substitution at the vinylene moieties of a series of stilbene derivatives in solution using the PCM method coupled with the TVCF approach. We found that the CN-substitution enhances molecular torsional motions of the single even double bonds neighbouring the CN group, *i.e.*, the single bonds adjacent to the CN groups in *α(β)*-CN-DSB and both the single and double bonds connected to the CN group in CN-BPPE, which opens the non-radiative decay channels and quenches the luminescence. The theoretically predicted fluorescence spectra and quantum efficiency are in good agreement with the experiments. Compared to the parent compounds, k_{nr} of the CN-substituents is increased by more than 4 orders of magnitude whereas k_r only slightly decreases, finally leading to the largely reduced Φ_f. Through analyses of the reorganization energies in mode and geometry relaxations, the non-radiative energy consumption channels of the CN-substituents are active via the above rotational movements in low-frequency regions and dihedral angles. Actually, there is not the only above-presented mechanism for the CN-substitution induced quenching phenomena. Gierschner et al. have stated that the

occurrence of a conical intersection (CI) is another possible reason although the precise description of the CI is theoretically unreachable for such large molecules [12]. Indeed, the non-radiative decay processes are rather complicated when they are tangled together. These non-radiative energy dissipation processes may partly or all participate in the quenching process. In this work, we simply emphasize only one aspect that the quenched emission arises from the rotation of CN-substituted neighbouring bonds, which we believe is essential for such series of molecules.

Finally, we should note that theoretical and computational investigations of excited-state dynamics consist of challenges [28,32,34]. The methodology we employed here has been based on a displaced and distorted harmonic oscillator model among other approximations. It is still a long way to go toward quantitative prediction of the optical emission spectra and quantum efficiency from first-principles.

Conflicts of interest

There are no conflicts to declare.

Appendix A. Supplementary data

Supplementary data to this article can be found online at https://doi.org/10.1016/j.orgel.2019.01.049.

References

[1] H. Wang, F. Li, I. Ravia, B.R. Gao, Y.P. Li, V. Medvedev, H.B. Sun, N. Tessler, Y.G. Ma, Cyano-substituted oligo(p-phenylene vinylene) single crystals: a promising laser material, Adv. Funct. Mater. 21 (2011) 3770–3777.

[2] L. Yuan, W.Y. Lin, K.B. Zheng, S.S. Zhu, FRET-based small-molecule fluorescent probes: rational design and bioimaging applications, Acc. Chem. Res. 46 (2013) 1462–1473.

[3] Z. Xu, M. Wang, J.S. Zhao, C.S. Cui, W.Y. Fan, J.F. Liu, Donor-acceptor type neutral green polymers containing 2,3-di(5-methylfuran-2-yl) quinoxaline acceptor and different thiophene donors, Electrochim. Acta 125 (2014) 241–249.

[4] J. Mei, N.L.C. Leung, R.T.K. Kwok, J.W.Y. Lam, B.Z. Tang, Aggregation-induced emission: together we shine, united we soar!, Chem. Rev. 115 (2015) 11718–11940.

[5] J. Ding, H.Y. Li, C. Wang, J. Yang, Y.J. Xie, Q. Peng, Q.Q. Li, Z. Li, "Turn-on" fluorescent probe for mercury(II): high selectivity and sensitivity and new design

approach by the adjustment of the π-bridge, ACS Appl. Mater. Interfaces 7 (2015) 11369–11376.

[6] L. Ma, Y. Yu, L. Li, T. Lei, B. Jiao, X. Hou, Z.X. Wu, Efficient amplified spontaneous emission based on π-conjugated fluorophore-cored molecules studied by density functional theory, Org. Electron. 57 (2018) 123–132.

[7] J.W. Chung, S.J. Yoon, B.K. An, S.Y. Park, High-contrast on/off fluorescence switching via reversible E–Z isomerization of diphenylstilbene containing the α-cyanostilbenic moiety, J. Phys. Chem. C 117 (2013) 11285–11291.

[8] F. Ito, J.I. Fujimori, N. Oka, M. Sliwa, C. Ruckebusch, S. Ito, H. Miyasaka, AIE phenomena of a cyanostilbene derivative as a probe of molecular assembly processes, Faraday Discuss 196 (2017) 231–243.

[9] D. Oelkrug, A. Tompert, J. Gierschner, H.J. Egelhaaf, M. Hanack, M. Hohloch, E. Steinhuber, Tuning of fluorescence in films and nanoparticles of oligophenylenevinylenes, J. Phys. Chem. B 102 (1998) 1902–1907.

[10] B.K. An, S.K. Kwon, S.D. Jung, S.Y. Park, Enhanced emission and its switching in fluorescent organic nanoparticles, J. Am. Chem. Soc. 124 (2002) 14410–14415.

[11] S.J. Yoon, S.Y. Park, Polymorphic and mechanochromic luminescence modulation in the highly emissive dicyanodistyrylbenzene crystal: secondary bonding interaction in molecular stacking assembly, J. Mater. Chem. 21 (2011) 8338–8346.

[12] J.Q. Shi, L.E. Aguilar Suarez, S.J. Yoon, S. Varghese, C. Serpa, S.Y. Park, L. Lüer, D. Roca-Sanjuán, B. Milián-Medina, J. Gierschner, Solid state luminescence enhancement in π-conjugated materials: unraveling the mechanism beyond the framework of AIE/AIEE, J. Phys. Chem. C 121 (2017) 23166–23183.

[13] S. Nishio, K. Higashiguchi, K. Matsuda, The effect of cyano substitution on the fluorescence behavior of 1,2-bis(pyridylphenyl)ethene, Asian J. Org. Chem. 3 (2014) 686–690.

[14] Y.P. Li, F. Li, H.Y. Zhang, Z.Q. Xie, W.J. Xie, H. Xu, B. Li, F.Z. Shen, L. Ye, M. Hanif, D.G. Ma, Y.G. Ma, Tight intermolecular packing through supramolecular interactions in crystals of cyano substituted oligo(para-phenylene vinylene): a key factor for aggregation-induced emission, Chem. Commun. (2007) 231–233.

[15] C.F. Feng, K. Wang, Y.X. Xu, L.Q. Liu, B. Zou, P. Lu, Unique piezochromic fluorescence behavior of organic crystal of carbazole-substituted CNDSB, Chem. Commun. 52 (2016) 3836–3839.

[16] W.Z. Yuan, Y. Gong, S. Chen, X.Y. Shen, J.W.Y. Lam, P. Lu, Y. Lu, Z. Wang, R. Hu, N. Xie, H.S. Kwok, Y. Zhang, J.Z. Sun, B.Z. Tang, Efficient solid emitters with aggregation-induced emission and intramolecular charge transfer characteristics: molecular design, synthesis, photophysical behaviors, and OLED application, Chem. Mater. 24 (2012) 1518–1528.

[17] S.J. Yoon, J.W. Chung, J. Gierschner, K.S. Kim, M.G. Choi, D. Kim, S.Y. Park, Multistimuli two-color luminescence switching via different slip-stacking of highly fluorescent molecular sheets, J. Am. Chem. Soc. 132 (2010) 13675–13683.

[18] W.Z. Yuan, Y.Q. Tan, Y.Y. Gong, P. Lu, J.W.Y. Lam, X.Y. Shen, C.F. Feng, H.H.Y. Sung, Y.W. Lu, I.D. Williams, J.Z. Sun, Y.M. Zhang, B.Z. Tang, Synergy between twisted conformation and effective intermolecular interactions: strategy for efficient mechanochromic luminogens with high contrast, Adv. Mater. 25 (2013) 2837–2843.

[19] C. Adamo, V. Barone, Toward reliable density functional methods without adjustable parameters: the PBE0 model, J. Chem. Phys. 110 (1999) 6158–6170.

[20] D. Jacquemin, V. Wathelet, E.A. Perpète, C. Adamo, Extensive TD-DFT benchmark: singlet-excited states of organic molecules, J. Chem. Theory Comput. 5 (2009)

2420–2435.

[21] T. Zhang, Q. Peng, C.Y. Quan, H. Nie, Y.L. Niu, Y.J. Xie, Z.J. Zhao, B.Z. Tang, Z.G. Shuai, Using the isotope effect to probe an aggregation induced emission mechanism: theoretical prediction and experimental validation, Chem. Sci. 7 (2016) 5573–5580.

[22] A.D. Boese, J.M.L. Martin, Development of density functionals for thermochemical kinetics, J. Chem. Phys. 121 (2004) 3405–3416.

[23] J. Tomasi, B. Mennucci, R. Cammi, Quantum mechanical continuum solvation models, Chem. Rev. 105 (2005) 2999–3094.

[24] R. Improta, V. Barone, G. Scalmani, M.J. Frisch, A state-specific polarizable continuum model time dependent density functional theory method for excited state calculations in solution, J. Chem. Phys. 125 (2006) 054103.

[25] M.J. Frisch, G.W. Trucks, H.B. Schlegel, G.E. Scuseria, M.A. Robb, J.R. Cheeseman, G. Scalmani, V. Barone, G.A. Petersson, H. Nakatsuji, X. Li, M. Caricato, A.V. Marenich, J. Bloino, B.G. Janesko, R. Gomperts, B. Mennucci, H.P. Hratchian, J.V. Ortiz, A.F. Izmaylov, J.L. Sonnenberg, D. Williams-Young, F. Ding, F. Lipparini, F. Egidi, J. Goings, B. Peng, A. Petrone, T. Henderson, D. Ranasinghe, V.G. Zakrzewski, J. Gao, N. Rega, G. Zheng, W. Liang, M. Hada, M. Ehara, K. Toyota, R. Fukuda, J. Hasegawa, M. Ishida, T. Nakajima, Y. Honda, O. Kitao, H. Nakai, T. Vreven, K. Throssell, J.A. Montgomery Jr., J.E. Peralta, F. Ogliaro, M.J. Bearpark, J.J. Heyd, E.N. Brothers, K.N. Kudin, V.N. Staroverov, T.A. Keith, R. Kobayashi, J. Normand, K. Raghavachari, A.P. Rendell, J.C. Burant, S.S. Iyengar, J. Tomasi, M. Cossi, J.M. Millam, M. Klene, C. Adamo, R. Cammi, J.W. Ochterski, R.L. Martin, K. Morokuma, O. Farkas, J.B. Foresman, D.J. Fox, Gaussian16 Revision A.03, Gaussian, Inc., Wallingford, CT, 2016.

[26] Z.D. Li, Y.L. Xiao, W.J. Liu, On the spin separation of algebraic two-component relativistic Hamiltonians, J. Chem. Phys. 137 (2012) 154114.

[27] Y.L. Niu, W.Q. Li, Q. Peng, H. Geng, Y.P. Yi, L.J. Wang, G.J. Nan, D. Wang, Z.G. Shuai, Molecular materials property prediction package (MOMAP) 1.0: a software package for predicting the luminescent properties and mobility of organic functional materials, Mol. Phys. 116 (2018) 1078–1090.

[28] Z.G. Shuai, Q. Peng, Organic light-emitting diodes: theoretical understanding of highly efficient materials and development of computational methodology, Natl. Sci. Rev. 4 (2017) 224–239.

[29] S.H. Lin, Rate of interconversion of electronic and vibrational energy, J. Chem. Phys. 44 (1966) 3759–3767.

[30] Q. Peng, Y.P. Yi, Z.G. Shuai, J.S. Shao, Toward quantitative prediction of molecular fluorescence quantum efficiency: role of duschinsky rotation, J. Am. Chem. Soc. 129 (2007) 9333–9339.

[31] Y.L. Niu, Q. Peng, C.M. Deng, X. Gao, Z.G. Shuai, Theory of excited state decays and optical spectra: application to polyatomic molecules, J. Phys. Chem. A 114 (2010) 7817–7831.

[32] Z.G. Shuai, Q. Peng, Excited states structure and processes: understanding organic light-emitting diodes at the molecular level, Phys. Rep. 537 (2014) 123–156.

[33] J.R. Reimers, A practical method for the use of curvilinear coordinates in calculations of normal-mode-projected displacements and duschinsky rotation matrices for large molecules, J. Chem. Phys. 115 (2001) 9103–9109.

[34] Z.G. Shuai, D. Wang, Q. Peng, H. Geng, Computational evaluation of optoelectronic properties for organic/carbon materials, Acc. Chem. Res. 47 (2014) 3301–3309.